Official Journal of CIOMP
elight.springeropen.com

RESEARCH ARTICLE

Open Access

A large field-of-view, single-cell-resolution two- and three-photon microscope for deep and wide imaging

Aaron T. Mok[1,2*], Tianyu Wang[3*], Shitong Zhao[1], Kristine E. Kolkman[4], Danni Wu[5], Dimitre G. Ouzounov[1], Changwoo Seo[6], Chunyan Wu[7], Joseph R. Fetcho[4] and Chris Xu[1*]

Abstract

In vivo imaging of large-scale neuronal activity plays a pivotal role in unraveling the function of the brain's circuitry. Multiphoton microscopy, a powerful tool for deep-tissue imaging, has received sustained interest in advancing its speed, field of view and imaging depth. However, to avoid thermal damage in scattering biological tissue, field of view decreases exponentially as imaging depth increases. We present a suite of innovations to optimize three-photon microscopy for large field-of-view imaging at depths unreachable by two-photon microscopy. These techniques enable us to image neuronal activities of transgenic animals expressing protein calcium sensors in a ~ 3.5-mm diameter field-of-view with single-cell resolution in the deepest cortical layer of mouse brains. We further demonstrate simultaneous large field-of-view two-photon and three-photon imaging, subcortical imaging in the mouse brain, and whole-brain imaging in adult zebrafish. The demonstrated techniques can be integrated into typical multiphoton microscopes to enlarge field of view for system-level neural circuit research.

Keywords Three-photon microscopy, Two-photon microscopy, Large field of view, Brain imaging, DEEPscope

*Correspondence:
Aaron T. Mok
tm624@cornell.edu
Tianyu Wang
wangty@bu.edu
Chris Xu
cx10@cornell.edu
[1] School of Applied and Engineering Physics, Cornell University, Ithaca, NY, USA
[2] Meining School of Biomedical Engineering, Cornell University, Ithaca, NY, USA
[3] Department of Electrical and Computer Engineering, Boston University, Boston, MA, USA
[4] Department of Neurobiology and Behavior, Cornell University, Ithaca, NY, USA
[5] Harvard T.H. Chan School of Public Health, Harvard University, Cambridge, MA, USA
[6] Department of Molecular & Cellular Biology, Harvard University, Cambridge, MA, USA
[7] McGovern Institute for Brain Research at MIT, Cambridge, MA, USA

1 Introduction

Large field-of-view (LFOV) deep imaging with high spatial and temporal resolution in intact tissues is invaluable across many biological fields [1–7]. Recent advancements in two-photon microscopy (2PM) [1, 2, 4, 6–12] have enabled LFOV neural activity recordings up to approximately $5.4 \times 6 \times 0.5$ mm^3 at ~ 2 Hz [4]. However, the imaging depth remains limited to superficial cortical layers.

Three-photon microscopy (3PM) has reliably imaged neurons in deep cortical layers [13], subplates [14], and subcortex [3, 15, 16], providing optical access to regions beyond the reach of 2PM [17]. However, 3PM requires low laser repetition rates to avoid tissue thermal damage, which in turn limits the number of pixels that can be imaged per second. This constraint restricts 3PM imaging throughput, confining neural activity imaging to small FOVs of a few hundred micrometers [17]. Recent developments in 3PM have demonstrated vasculature structural imaging with a 2×2 mm^2 FOV at an imaging

depth of 730 μm [2], and neuronal structural imaging with a 0.2×0.2 mm^2 FOV at an imaging depth of 1.4 mm [13] in the intact mouse brain. For neural activity imaging, the FOV is approximately 0.34×0.34 mm^2 at an imaging depth of 1,000 to 1,220 μm [3, 18–21].

The challenge of realizing LFOV 3PM lies in the efficiency of fluorescence signal generation. In fact, fluorescence signal generation in LFOV and deep imaging presents significant challenges for both 2PM and 3PM techniques. While LFOV 2PM can be achieved with a lower optical resolution to increase imaging throughput, this approach cannot be applied to 3PM. Since 3PM relies on higher-order nonlinear excitation compared to 2PM, an enlarged excitation profile would greatly reduce 3PM excitation efficiency [22], further reducing the FOV of 3PM.

We have developed a Dual Excitation with adaptive Excitation Polygon-scanning multiphoton microscope (DEEPscope) with optimized multiphoton fluorescence signal generation efficiency to overcome some of the previous constraints on the imaging depth of 2PM and imaging FOV of 3PM to achieve deep LFOV imaging in transgenic animals. We introduced a suite of innovations, including (1) adaptive excitation to reduce the average power required, (2) multi-focus excitation profile optimization for high fluorescence generation efficiency, and (3) a polygon scanning scheme for large-angle high-speed scanning. These innovations optimized fluorescence generation per laser pulse for 3PM to allow LFOV 3PM imaging and to image beyond the repetition rate of commercial lasers and the scanning throughput of mechanical scanners.

2 Results

2.1 DEEPscope for large-field-of-view imaging deep in scattering tissue

We developed DEEPscope that achieves single-cell-resolution imaging with a large FOV of 3.5 mm in diameter deep in scattering tissue. Figure 1 shows the experimental setup utilizing both 2P and 3P excitation. The 3P excitation path consists of an adaptive excitation module, a beamlet generation delay line, and a scan engine with a polygon scanner. The 2P excitation path consists of an adaptive excitation module, a remote focusing module, and utilizes the same polygon scan engine as 3P excitation. The DEEPscope achieved deep and LFOV imaging in scattering brain tissues by (1) reducing the power required for LFOV imaging using adaptive excitation, (2) improving the excitation efficiency and scanning speed using optimized PSF and beamlets, and (3) performing fast and large-angle optical scans using the polygon scanner.

While polygon-scanning multiphoton microscopes have been demonstrated before, the FOV is relatively small (~512×512 μm) [23, 24]. We used a polygon scanner to achieve a large scan angle at high scanning speed, which also reduces the complexity of the scanning engine when compared to the existing LFOV microscopes [1, 6, 9]. The optical path and the footprint for the DEEPscope (~3 ft×3 ft×1 ft, Supplementary Fig. 1) are nearly identical to a conventional multiphoton microscope. The polygon scanner has a larger aperture (9.5 mm) and more than twice the optical scan angle (~42-degree peak-to-peak at 70% duty cycle) of a resonant galvanometer scanner. The polygon line rate (~6 kHz) is >6 times that of 5-mm aperture galvo scanners (<1 kHz) at the same optical scan angle.

2.2 Adaptive excitation and beamlet scanning for improving the multiphoton excitation efficiency

To reduce the average power required for LFOV 2P and 3P imaging, an adaptive excitation scheme [25] enabled by electro-optical modulators (EOMs) was used to block the laser in areas where large blood vessel shadows were located. Figure 1c shows an image of cortical layer 6 (L6) with and without adaptive excitation. Fluorescence intensity, shown as the gray level intensity, increased during adaptive excitation. This is attributed to the higher effective power (224 mW) across the regions of interest when adaptive excitation was applied, compared to the non-adaptive excitation condition (130 mW). The effective power is calculated as the average power on the brain surface (119 mW) divided by the adaptive excitation duty cycle (53%). Importantly, this increase in fluorescence intensity was achieved with a lower overall average power on the brain surface compared to non- adaptive excitation condition.

To optimize excitation efficiency and improve imaging speed using a low repetition rate laser, we employed a beamlet scanning scheme with a point spread function (PSF) optimized to the size of neurons. A higher excitation efficiency improves the detection fidelity of calcium transients, which can be quantified using a discriminability index (d') [26]. For an optimized d', we underfilled the back aperture of the DEEPscope objective (~85% filled using the $1/e^2$ radius of the excitation beam) to achieve a numerical aperture (NA) of around 0.58, i.e. axial resolution across the FOV of ~5 μm full-width half maximum (FWHM) (Supplementary Fig. 2) and 0.7 μm FWHM lateral resolution. This size of the PSF is close to the optimum for the size of neuron cell bodies, and approximately doubled d' value by increasing the fluorescence signal ~4 times when compared to a PSF with a 2-μm axial resolution (Supplementary Fig. 3) with the same target fluence. This result is consistent with other studies

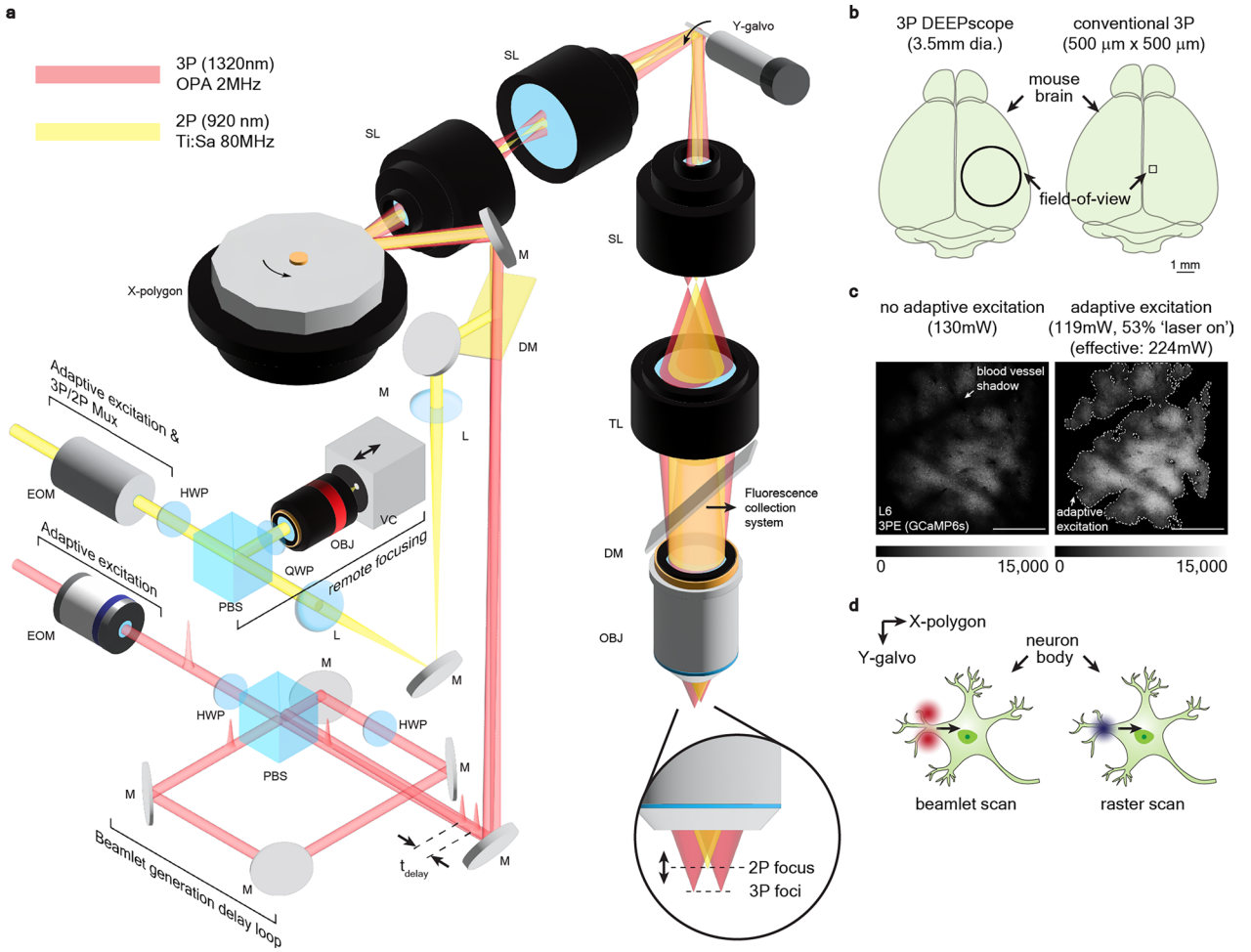

Fig. 1 Dual-beam Excitation with adaptive Excitation Polygon-scanning multiphoton microscope (DEEPscope). **a** DEEPscope schematics. The 3P path consists of an adaptive excitation module, a beamlet generation delay loop, and a scan engine with a polygon scanner. The 2P path consists of an adaptive excitation module, a 3P/2P multiplexing module, a remote focusing module, and the same scan engine as for 3P imaging. **b** Comparison of the FOV of 3P DEEPscope with conventional 3P microscopes. DEEPscope images 3.5 mm diameter FOV in the mouse brain. **c** Comparison of fluorescence intensity across the FOV with and without adaptive excitation at similar average excitation power. Grayscale bar shows pixel intensity. Scale bar, 1 mm. **d** Schematic of beamlet scanning with the beamlet generation delay loop. *EOM* electro-optic modulator, *HWP* half-wave plate, *QWP* quarter wave-plate, *PBS* polarization beam splitter, *VC* voice coil, *L* lens, *M* mirror, *SL* scan lens, *TL* tube lens, *DM* dichroic mirror, *OBJ* objective, *Mux* multiplexing, t_{delay} time delay between the pulses of the two beamlets

[3]. In addition, we created a beamlet scanning scheme in which two pulses were scanned in two adjacent lines with a time delay of ~ 20 ns (Fig. 1d). Such a two-beamlet scanning scheme with two 5-μm axial resolution PSF further increased d' value by ~ 10% (fluorescence signal by ~ 20%) when compared to scanning with a PSF with 10-μm axial resolution, while both configurations require the same power for the same target fluence. Furthermore, the beamlets doubled the effective laser repetition rate and the line scanning speed, resulting in doubling both the spatial and the temporal resolution. Further increasing the number of beamlets can be advantageous if an excitation source with higher pulse energy at the same repetition rate is available, providing greater gains in d' value and higher spatial and temporal resolution (Supplementary Fig. 3).

2.3 Single-cell resolution, large-field-of-view 3P imaging in cortical L6 and deep imaging in CA1 through intact Cortex

We performed 3P LFOV structural imaging of neurons in a cortical column and the stratum pyramidale (SP) layer of the CA1 region of the hippocampus in a transgenic mouse (Fig. 2 and Supplementary Video 1). We scanned a 3.23 mm × 3.23 mm field to cover most of the 3.5-mm diameter FOV of the microscope. We imaged a

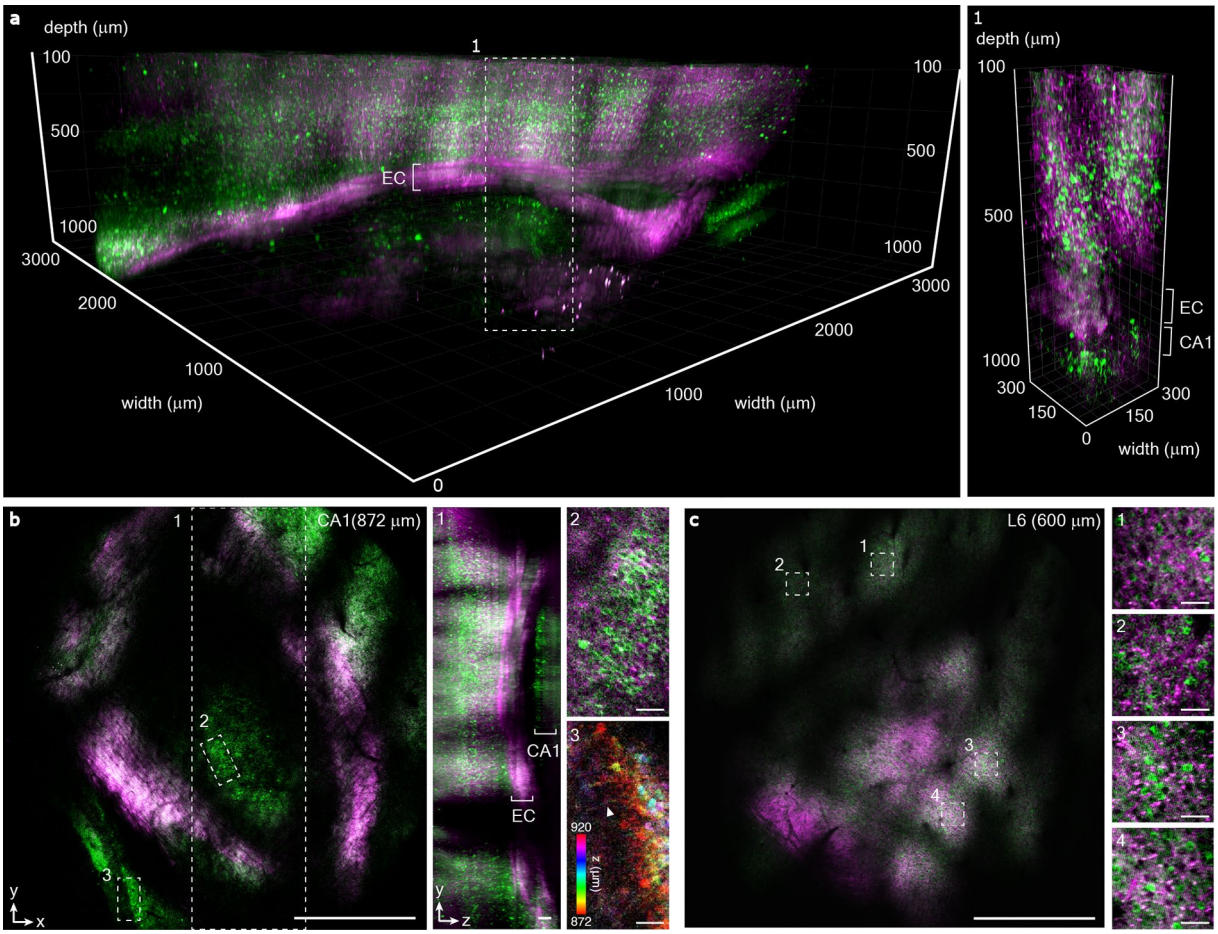

Fig. 2 Deep and LFOV *in-vivo* imaging of mouse brain structures. **a** 3D rendering of GCaMP6s-expressing neurons by 3P DEEPscope from 100 to 1,048 μm below the brain surface (*CamKII-tTa/tetO-GCaMP6s mouse*, male, 16-week-old). The scanning field was 3.23 mm × 3.23 mm, acquired with 0.8-μm pixel size and a z-step of 4 μm. The integration time per imaging depth was 1.5 min, 4 min, and 10 min at the depth of 100–900 μm, 900–950 μm, and 950–1,048 μm respectively. Panel 1 shows the digitally zoomed-in volume of the 3D stack in **a** (indicated by the white dashed box) with 300 μm FOV. **b** Selected 2D images from **a** of CA1 hippocampal neurons at an imaging depth of 872 μm. Panel 1 shows the YZ maximum intensity projection of the dashed box 1 in (**b**). Panels 2 and 3 show digitally zoomed-in images of the corresponding white dashed boxes in (**b**). White arrowhead points to an axon. Scale bar in (**b**), 1 mm. Scale bar in panel 1, 100 μm. Scale bars in panels 2 and 3, 50 μm. **c** Selected 2D image from **a** of layer 6 neurons at an imaging depth of 600 μm. Panels 1–4 show digitally zoomed-in images of the corresponding dashed white boxes in **c**. Scale bar of c, 1 mm. Scale bars in panels 1 to 4, 50 μm. *EC* external capsule, LFOV and zoomed-in images in (**b**) and (**c**) have different linear contrast stretch for visualization

stack from 100 to 1,048 μm in depth (Fig. 2a and Supplementary Video 2). GCaMP6s-expressing neurons in the SP layer appear at ~ 872 μm depth (Fig. 2b). The external capsule (EC), where myelinated axons produce strong third harmonic generation (THG) signals, appeared to be curved across the LFOV and extended from ~ 600 μm to 1,048 μm below the brain surface (Fig. 2b). After the image acquisition, the digitally zoomed-in images and video (Fig. 2b, c, Supplementary Video 1 and Supplementary Video 2) show the labeled neurons with clear nuclear exclusion in the whole cortical column and sub-cortical region. We also measured an axial resolution of ~ 5 μm in a vasculature-labeled mouse at a depth of 800 μm below the brain surface (Supplementary Fig. 4), which provides an estimate for the axial resolution at one specific location within the FOV. While not measured, we believe the axial resolution may vary across the LFOV when imaging deep in the tissue. Figure 2 shows that 3P DEEPscope is capable of high-resolution, large FOV imaging deep within intact mouse brains.

We imaged the spontaneous activity of GCaMP6s-expressing neurons in adult transgenic mice in the cortical L6 to demonstrate the capability of the 3P DEEPscope for LFOV activity imaging in the deep cortical regions. Figure 3a shows the 3.23 mm × 3.23 mm scanned field and the digitally zoomed-in imaging sites in cortical L6

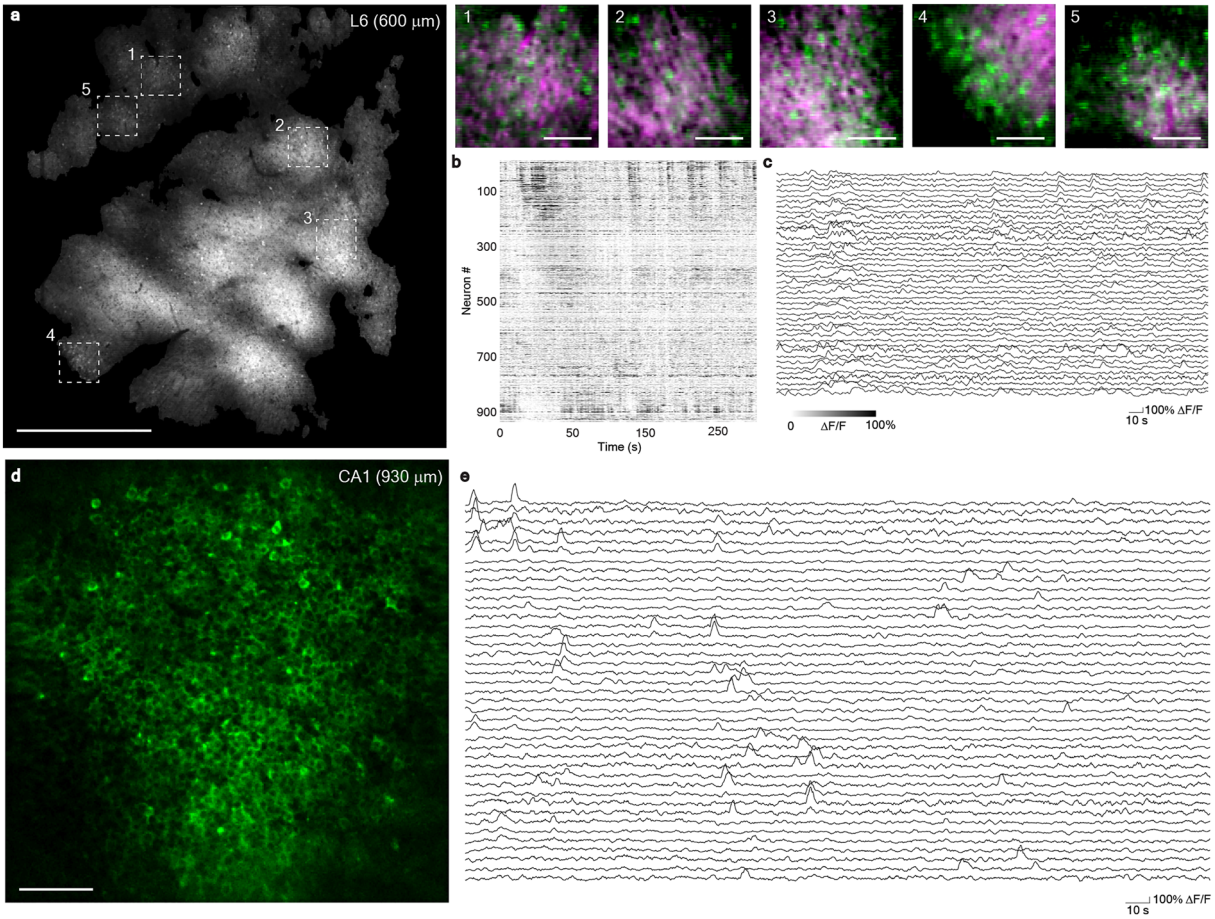

Fig. 3 1320 nm 3P activity imaging with DEEPscope. **a** 3PM image of an activity recording site in an awake, GCaMP6s-expressing transgenic mouse (*CamKII-tTa/tetO-GCaMP6s*, male, 15-week-old). The recording site is 600 m below the brain surface, right above EC, with a scanning field of 3.23 mm × 3.23 mm. Panels 1–5 show digitally zoomed-in images from the corresponding white dashed boxes in **a**. Scale bar, 1 mm. Scale bars in panels 1 to 5, 100 m. **b** Spontaneous activity traces recorded under awake conditions from 917 neurons in **a**. The average power on the brain surface was 119 mW. 53% of the scanned area was excited using the adaptive excitation scheme. The recordings were acquired with 1030 × 1030 pixels per frame (a pixel size of 3.14 m) and a nominal frame rate of 4 Hz using two beamlets and the polygon scanner. **c** Selected activity traces from (**b**). **d** Image of an activity recording site in an awake, GCaMP6s-expressing transgenic mouse (*CamKII-tTa/tetO-GCaMP6s*, female, 17-week-old). The imaging took place in the sixth week after cranial window implantation. The recording site is at 930 µm below the brain surface with a FOV of 550 µm × 550 µm. Scale bar, 100 µm. **e** Selected spontaneous activity traces recorded from 42 active neurons (out of 503 segmented neurons) in the FOV under awake condition. The repetition rate used for imaging was 1 MHz and the average power on the brain surface was 120 mW. The recordings are acquired with 512 × 512 pixels per frame, a pixel size of 1.06 µm, and at 4.3 Hz frame rate using a galvo-galvo scanner

at 600 µm depth, right above the EC. We used adaptive excitation to reduce the average excitation power from 224 mW to 119 mW while keeping the same pulse energy at the regions of interest. The pulse energy on the brain surface is 56 nJ. We recorded neuronal activity traces from a large population of neurons (917 neurons) in an awake mouse (Fig. 3b and Supplementary Video 3) at a scanning frame rate of 4 Hz. This frame rate is enabled by the polygon scanner with the two beamlets, which matches the scan throughput to the imaging FOV. However, the effective frame rate is limited to 2.6 Hz (i.e., every pixel is illuminated by ~ 2.6 pulses/s), due to the repetition rate limitations of the laser. Figure 3c shows selected activity traces of the neurons. The raw photon counts during the activity recordings, shown in Supplementary Fig. 5, indicate an average of 58 photons per neuron per second, corresponding to a d' of approximately 2.3. This photon signal falls within the expected range of the calculated value (see Supplementary Note 1). This reflects a modest decrease in d' compared to conventional 3P imaging, where d' of around 3 is typically obtained in the same GCaMP6s transgenic mice [17].

We also imaged hippocampal SP neurons at 930 µm depth with a FOV of 550 µm × 550 µm. The FOV for

hippocampal imaging was reduced due to the limit on laser average power to prevent tissue heating (Fig. 3d and Supplementary Video 4). Figure 3e shows the fluorescence time traces of the most active 42 neurons from the 503 identified hippocampal SP neurons.

2.4 2P and 3P dual excitation for large-field-of-view neuronal activity imaging at various depths

While 3P DEEPscope enables deep imaging in mice, 2P imaging achieves a higher volumetric imaging rate for shallow imaging depths due to its higher laser repetition rate [17]. Therefore, we designed the DEEPscope for excitation wavelengths of 910–930 nm, 1,030–1,050 nm, 1,240–1,380 nm, and 1,640–1,750 nm to enable both 2P shallow and 3P deep imaging. Supplementary Fig. 6 and Supplementary Fig. 7 show the transmission over the entire FOV for 920 nm and 1320 nm. Figure 4a shows an imaging site of L5 neurons 480 μm below the brain surface in an adult transgenic mouse. We recorded the neuronal activity traces of a large population of 2,000 neurons under awake conditions at a 6 Hz frame rate (Fig. 4c, d). By reducing the FOV to 3.23 mm × 1 mm, we performed high spatial-resolution activity imaging (0.67 μm pixel size) at a 4 Hz frame rate (Fig. 4b). Nuclear exclusion and dendrites of the labeled neurons are clearly visible. We recorded the neuronal activity traces of 503 neurons (Fig. 4e, f), which demonstrates that the DEEPscope can achieve high speed, LFOV, and high-resolution in 2P imaging.

We performed simultaneous six-plane 2P and 3P activity imaging of both shallow and deep cortical GCaMP6s-expressing neurons in adult transgenic mice. Figure 5 shows 3.23 mm × 3.23 mm FOV 2P imaging of five focal planes at 320, 340, 360, 380, 400 μm depth at a cycling rate of 2.2 Hz and 3P imaging at 600 μm depth at a scanning frame rate of 11 Hz. We were able to record neuronal activity traces from a large population of neurons (4,523 neurons) under awake conditions. Figure 5b, c show spontaneous activity traces recorded by 920-nm 2PM under awake conditions from five focal planes in the FOV. Figures 5d, e show spontaneous activity traces recorded by 1320-nm 3PM.

2.5 3P large field-of-view imaging of adult Zebrafish brain

The DEEPscope can be applied to other animal models as well. We performed 3P LFOV imaging of an adult zebrafish brain in vivo. We imaged a stack from 0 to 1,090 μm in depth (Fig. 6, Supplementary Videos 5, 6). Individual GCaMP6s-expressing nuclei were clearly visible in the telencephalic, optic tectum, and cerebellar regions, and the THG signal revealed bone structures and fiber tracts. The entire olfactory bulbs, the olfactory nerves, and parts of the olfactory epithelium were also visible.

3 Discussion

The DEEPscope offers a promising path towards achieving the full potential of multiphoton microscopy for LFOV, deep and high-resolution imaging of a large population of neurons. The utilization of a single set of polygon-galvo scanners greatly reduces the complexity of LFOV multiphoton imaging systems. The beamlet scanning and adaptive excitation schemes are modular, scalable, and can be readily integrated into typical multiphoton microscopes. Additionally, DEEPscope enables deep and LFOV imaging in transgenic mice, while virus injections are typically used previously for LFOV imaging [6, 8, 10] and hippocampal activity imaging [3, 15, 19] because labeled neurons with virus injection are typically brighter than those in transgenic mice. Although our current implementation uses customized components to optimize performance, the beamlet scanning and adaptive excitation schemes are independent of these components. In addition, these customized components are now commercially available, as detailed in Supplementary Table 1. The simplicity and compactness of DEEPscope enables straightforward implementation of LFOV deep imaging in biomedical research laboratories.

DEEPscope achieves a 3.23×3.23 mm^2 LFOV and is capable of deep neural activity imaging down to the deepest cortical layer, as well as structural imaging at depths greater than 1,000 μm. This increased the imaging area of 3PM by approximately two orders of magnitude. For 2P activity imaging, DEEPscope maintains a high lateral sampling of 0.67 μm pixel size with 0.7 μm PSF (FWHM), which allows visualization of dendrites during activity imaging. Moreover, DEEPscope supports simultaneous LFOV 2P and 3P imaging, which enables imaging of both superficial and deep cortical layers.

DEEPscope has demonstrated whole-brain structural imaging in model organisms beyond the mouse brain. While previous studies have achieved adult zebrafish brain imaging at a depth of around 1 mm with 200 μm FOV or around 850 μm depth with 500 μm FOV [27, 28], our work expands the capability for deeper and wider imaging in adult zebrafish. DEEPscope achieved an FOV greater than 3 mm and penetration depths exceeding 1 mm. This capability in adult zebrafish highlights DEEPscope's potential for broad applications across various model organisms or tissue samples, such as in lymph nodes [29] and tumors [30].

The capability of DEEPscope is ultimately constrained by the achievable fluorescence signal, which limits imaging depth, FOV, and throughput. For LFOV multiphoton imaging, the maximum number of pixels per second is

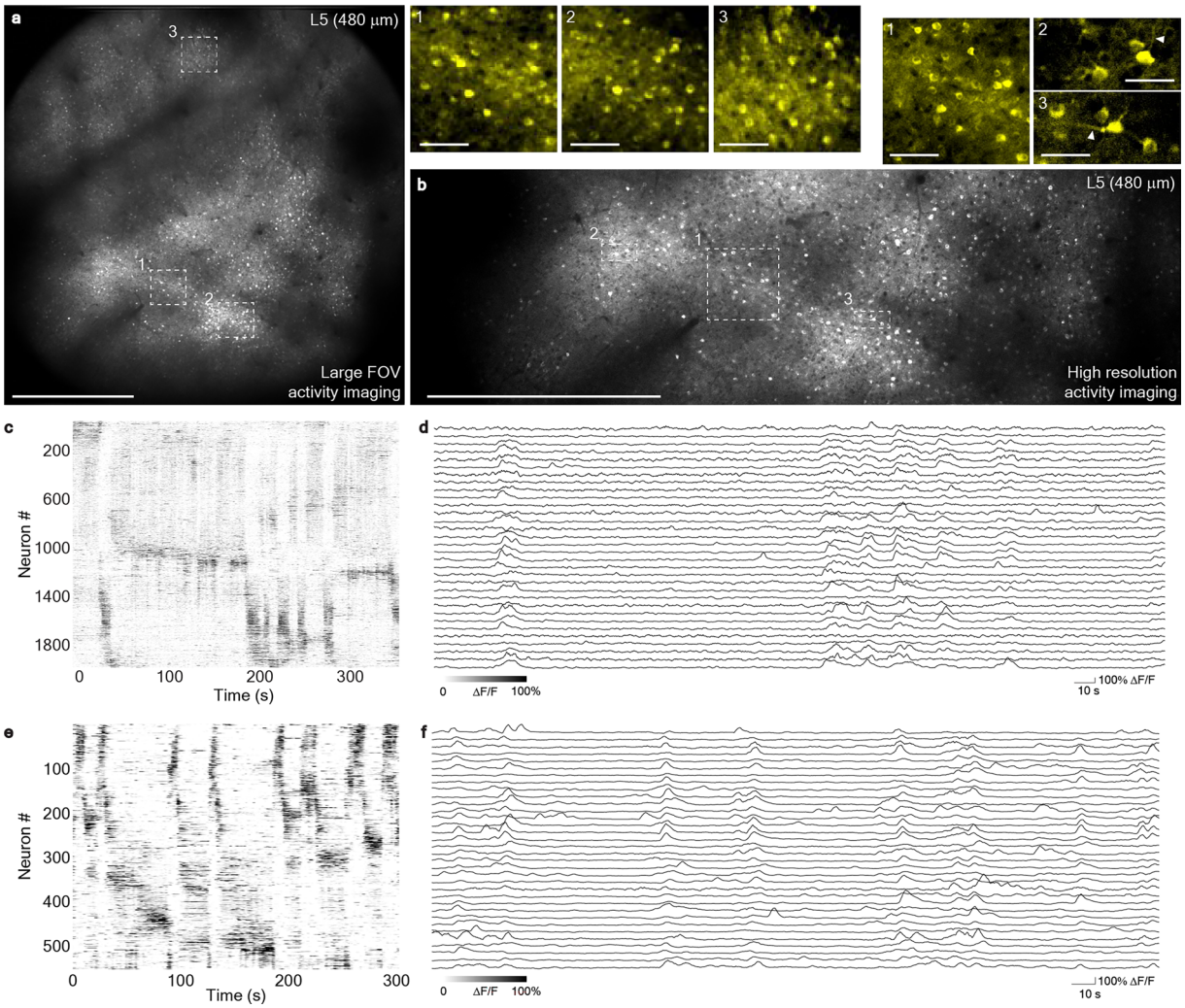

Fig. 4 920-nm 2P activity imaging with DEEPscope. Spontaneous activity recorded by 2P DEEPscope from cortical neurons (L5, 480 μm below the brain surface) in a GCaMP6s-expressing transgenic mouse under awake condition (*CamKII-tTA/tetO-GCaMP6s*, male, 14-week-old). The imaging took place in the second week after cranial window implantation. **a** Image of the recording site with a scanning field 3.23 mm × 3.23 mm acquired by 920-nm 2PM. Scale bar, 1 mm. Panels 1, 2 and 3 show digitally zoomed-in images of the corresponding white dashed boxes. Scale bar, 100 μm. The average power on the brain surface was 130 mW with a pulse repetition rate of 80 MHz. The recordings were acquired with 1042 × 1042 pixels per frame, 3.14 μm pixel size and at 5.76 Hz frame rate. **b** High-resolution image of the recording site with a scanning field 3.23 mm × 1 mm of cortical L5 neuron acquired by 920-nm 2PM as a part of the imaging site in (**a**). Scale bar, 1 mm. Panels 1, 2 and 3 show digitally zoomed-in images in the corresponding white dashed boxes in (**b**). Panel 1 in (**b**) is at the same region as panel 1 in (**a**). Scale bar in panel 1, 100 μm. Scale bar in panel 2 and 3, 50 μm. White arrowheads point to the dendrites. The average power on the brain surface was 130 mW with a repetition rate of 80 MHz. The recordings were acquired with 4862 × 1490 pixels per frame, 0.67 μm pixel-size and at 4.0 Hz frame rate. **c** Spontaneous activity traces recorded under awake conditions from 2000 neurons in the FOV in (**a**). **d** Selected activity traces from (**c**). **e** Spontaneous activity traces recorded under awake conditions from 503 neurons in the FOV in (**b**). **f** Selected activity traces from (**e**)

limited by the scanner throughput (i.e., the number of resolvable points scanned per second) and the laser repetition rate. By using a polygon scanner that is matched to the imaging FOV and two beamlets, we were able to achieve a sufficient scan throughput for LFOV at 4 Hz (Fig. 3a) or 11 Hz (Fig. 5) frame rate while maintaining cellular spatial resolution. The 11 Hz frame rate was chosen to accommodate 2P imaging of 5 axial planes. However, existing 3P laser source does not provide sufficient pulse energy to generate more than 2 beamlets with sufficient pulse repetition rate to match the performance of the scanning system. For 3P imaging in Figs. 3a and 5, the number of pulses per pixel is 0.645 and 0.235, respectively. Therefore, the repetition rate of our laser, with two beamlets, limits the 3P imaging to an effective frame rate of ~ 2.6 Hz (i.e., every pixel is illuminated

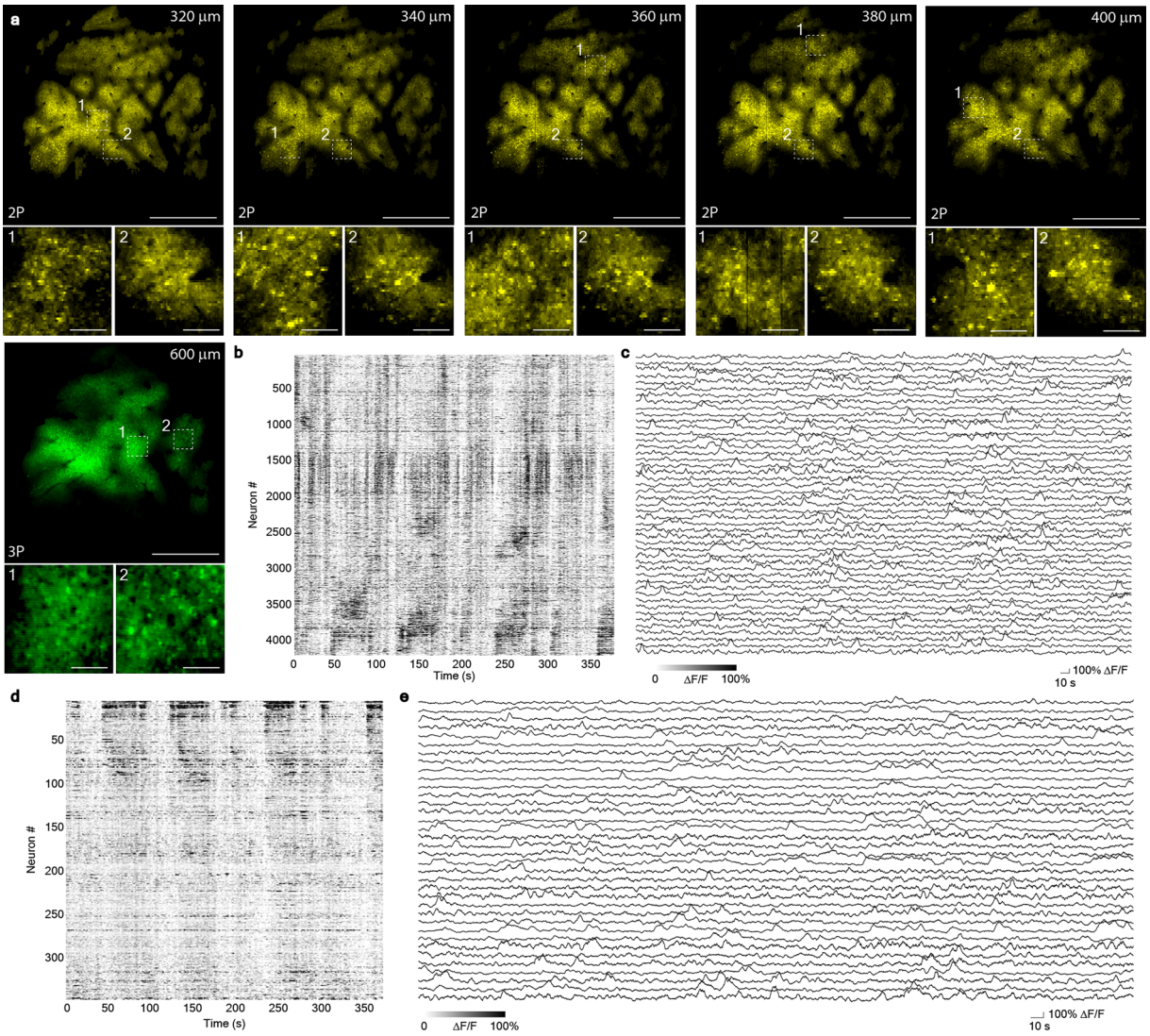

Fig. 5 LFOV neuronal activity recording in the shallow and deep cortex of GCaMP6s-expressing transgenic mouse. **a** Images of six focal planes acquired simultaneously by 1320-nm 3PM (green) and 920-nm 2PM (yellow) in an awake, GCaMP6s-expressing transgenic mouse (*CamKII-tTa/tetO-GCaMP6s*, female, 17-week-old). The activity recording sites were 320, 340, 360, 380, 400 and 600 µm below the brain surface with a scanning field of 3.23 mm × 3.23 mm. Scale bar, 1 mm. Panels 1 and 2 show digitally zoomed-in images from the corresponding white dashed boxes. Scale bar, 100 µm. **b** Spontaneous activity traces recorded by 920-nm 2PM under awake conditions from 4183 neurons (total from the five focal planes) in the FOV in (**a**). **c** Selected activity traces from (**b**). **d** Spontaneous activity traces recorded by 1320-nm 3PM under awake conditions from 340 neurons in the FOV in (**a**). **e** Selected activity traces from (**d**). For 3P imaging, the average power on the brain surface was 97 mW. 46% of the scanned area was excited using the adaptive excitation scheme. The recordings were acquired with 1030 × 1030 pixels per frame, a pixel size of 3.14 µm and a frame rate of 11 Hz using two beamlets. For 2P imaging, the laser repetition rate used for imaging was 80 MHz, and the average power on the brain surface was 75 mW. 62% of the scanned area was excited using the adaptive excitation scheme. The recordings were acquired with 1030 × 515 pixels per frame, a pixel size of 3.14 × 6.28 µm and a volume rate (i.e., the cycling rate among the five focal planes) of 2.2 Hz

by ~ 2.6 pulses/s) at 1030 × 1030 pixels/frame. Further optimization of the 3P source (higher repetition rate and/or higher pulse energy) can improve the performance of deep and LFOV imaging.

The current implementation of adaptive excitation suggests potential for further enhancing excitation efficiency. It would be advantageous to implement a customized adaptive excitation source (AES) that illuminates only the neurons with a high instantaneous repetition rate. As shown in a previous paper [25], it can increase the fluorescence signal by more than tenfold without increasing the average power. New transgenic mice with brighter jGCaMP7s or jGCaMP8s indicators will further increase fluorescence signal

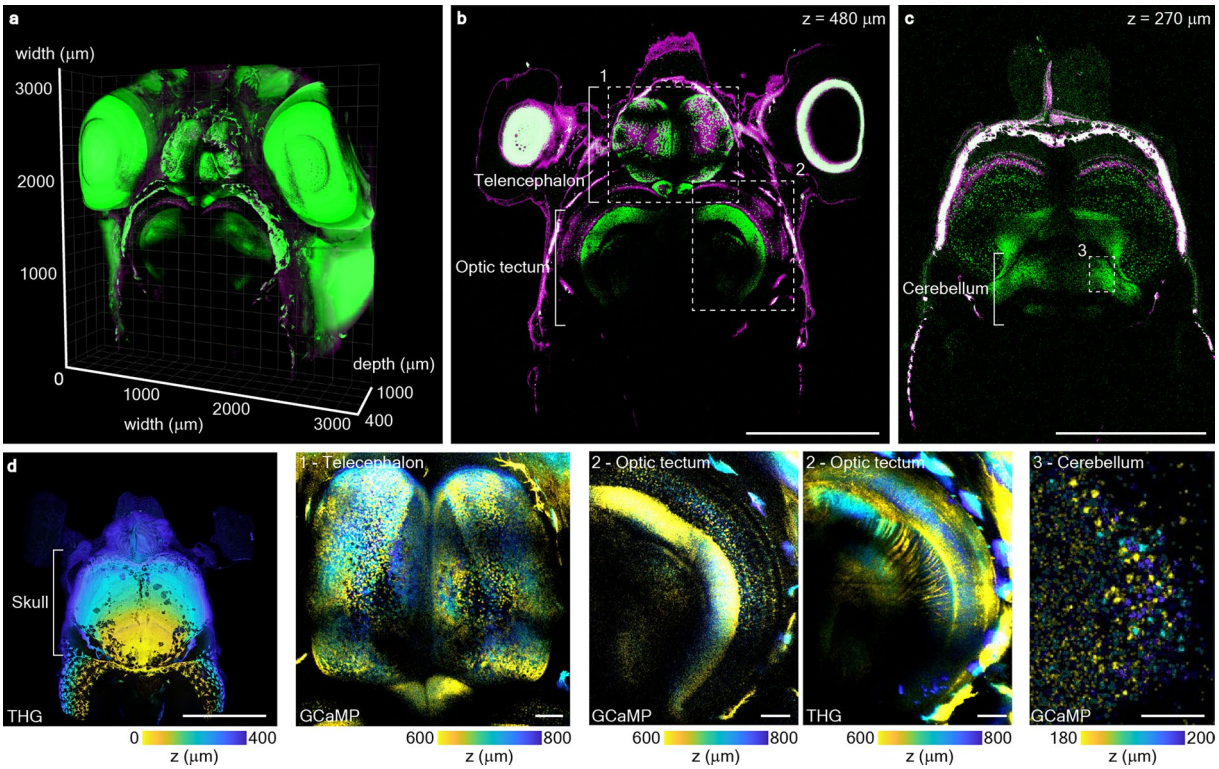

Fig. 6 Whole-brain imaging of a living, intact adult zebrafish. **a** 3D rendering of structural imaging of GCaMP6s-expressing nuclei (green) and THG signal (magenta) from regions with myelinated fibers obtained by 3P DEEPscope from 400 to 1090 μm below the surface of the skull bone of an adult zebrafish (Tg(elavl3::H2B-GCaMP6s, male, 9-months-old, 15.4-mm standard lengths). The scanning field is 3.23 mm × 3.23 mm, acquired with 0.8-μm pixel size and 10-μm z-step using the polygon scanner. **b** Image of the zebrafish at an imaging depth of 480 μm, showing the brain region telencephalon and optic tectum. GCaMP6s-expressing nuclei are shown in green and THG signal is shown in magenta. Scale bar, 1 mm. **c** Image of the zebrafish at an imaging depth of 270 μm, showing the brain region cerebellum. GCaMP6s- expressing nuclei are shown in green and THG signal is shown in magenta. Scale bar, 1 mm. **d** THG image of the zebrafish at the imaging depths of 0–400 μm, showing the skull bone. The color map shows the imaging depth. Scale bar, 1 mm. Panels 1, 2 and 3 show digitally zoomed-in images of the corresponding dashed white boxes in (**b**) and **c** with a color map showing the imaging depth. Scale bar, 100 μm. The integration time per imaging depth was 0.5 min, 1 min and 1.7 min at the depths of 0–750 μm, 760–900 μm and 910–1090 μm, respectively

by more than fourfold [31–33] for single and multiple action potentials. Better AES and brighter calcium indicators will further improve the capability of the DEEPscope for deep, fast, and LFOV imaging of neuronal activity.

The calculated maximum fluence at focus used in this study is approximately 4.7 nJ/μm^2, which is higher than the targeted 3 nJ/μm^2 as stated in Supplementary Fig. 3; however, this maximum fluence is calculated without considering variations in aberration, scattering length and power transmission (e.g., blood vessel shadows) across the FOV, which can cause significant signal variations across the LFOV (Supplementary Fig. 8). The maximum fluence in our experiments is chosen to accommodate the variations across the LFOV and ensure that neurons located in the dim regions are also captured. We note that the maximum fluence used in this study is still below the damage threshold for peak intensity in mouse brains [14].

In this study, chronic craniotomy was performed on mice, with imaging conducted 2–8 weeks after cranial window implantation. Alternative approaches, such as the skull optical clearing window and imaging through the intact skull, could allow for immediate imaging post-skull preparation. The skull optical clearing window technique, which avoids cortical inflammation, has been demonstrated to enable high-resolution and deep imaging shortly after preparation using 3PM [34–38]. Similarly, 3P imaging through the intact skull allows for cortical structural and functional imaging without the need for craniotomy [39, 40]. DEEPscope is compatible with both skull optical clearing and imaging through the intact skull.

4 Materials and methods

4.1 Dual excitation with adaptive excitation polygon-scanning multiphoton microscope (DEEPscope)

Excitation source and adaptive excitation. The excitation source for 3PM was a noncollinear optical parametric amplifier (NOPA, Spectra-Physics) pumped by an amplifier (Spirit, Spectra-Physics). The NOPA operated at a center wavelength of 1320 nm and provided an average power of ~ 2 W at ~ 2 MHz repetition rate (~ 1 μJ per pulse). It was paired with an electro-optic modulator (EOM) (360–40-03, Conoptics) for adaptive excitation [25]. A two-prism (SF11 glass) compressor was used to compensate for the normal dispersion of the optics in the light source and the microscope. The pulse duration (measured by second-order interferometric autocorrelation) under the objective was ~ 60 fs after dispersion compensation.

The excitation source for 2PM was a mode-locked Ti:Sapphire laser (Chameleon, Coherent). The Ti:Sapphire laser operated at a center wavelength of 920 nm and provided an average power of ~ 1.6 W at 80 MHz repetition rate. It was paired with an EOM (350–160, Conoptics) for adaptive excitation. A two-prism (SF11 glass) compressor was used to compensate for the normal dispersion of the optics in the light source and the microscope. The pulse duration (measured by second-order interferometric autocorrelation) under the objective was ~ 90 fs after dispersion compensation.

Beamlet generation delay line. A beamlet generation delay line (Fig. 1) was used to split a laser pulse at 1320 nm into two pulses (beamlets) with ~ 20 ns time delay, increasing the effective laser repetition rate from ~ 2 MHz to ~ 4 MHz. The delay line was arranged as a loop with four one-inch dielectric mirrors (102077, Layertec) and a polarizing beam splitter cube (PBS) (PBS103, Thorlabs). The PBS served as the input and output port of the delay line. The power distribution of each beamlet was controlled by adjusting the half-wave plate (HWP) (WPH05M-1310, Thorlabs) before the PBS. Inside the loop, two mirrors were tilted to adjust the angular separation between the beamlets. The angularly separated beamlets converge on the polygon scanner in a plane that was perpendicular to the scanning direction. An 8-f system was placed inside the loop to compensate for the difference in beam divergence between the beamlets. Two co-planar foci that were ~ 3 μm apart was created along the slow Y-axis (Supplementary Fig. 9). Alignment procedures for the beamlet generation delay line are described in Supplementary Note 2. The fluorescence signal generated by the two beamlets is demultiplexed temporally and forms the pixels in the corresponding lines in the image. The crosstalk of the fluorescence signals between the two beamlets was measured to be ~ 5%, which was caused by the data acquisition bandwidth of the system (Supplementary Fig. 10).

DEEPscope setup. We developed a multiphoton microscope that enables 3.5 mm diameter LFOV imaging (Supplementary Fig. 11) using a custom-designed scan lens (f = 60 mm), tube lens (f = 200 mm), and objective lens (f = 15 mm) (Special Optics, Navitar). The objective lens is water immersion and has a maximum excitation NA of 0.75 and a collection NA of 1.0 (Supplementary Fig. 12) with a 2.8 mm working distance. The objective was underfilled with $1/e^2$ beam diameter of ~ 17 mm to achieve NA ~ 0.58 with an axial resolution (FWHM) of ~ 5 μm and lateral resolution (FWHM) of ~ 0.7 μm across the FOV (Supplementary Fig. 2 and Supplementary Fig. 9) for both 2P excitation at 920 nm and 3P excitation at 1320 nm. A 9-mm aperture polygon scanner and a 10-mm aperture galvo-mirror (Saturn 9B, ScannerMax) were conjugated using two custom-designed scan lenses (f = 60 mm) (Special Optics, Navitar) (Fig. 1). The customized polygon scanner (PT60SRG, Nidec Copal Electronics) has 12 facets, each with 17.5 mm × 9.5 mm clear aperture. Since beam truncation occurs at the edge of each facet, the fill fraction of the polygon scan was 70% to ensure uniform transmission across the FOV. A 42-degree peak-to-peak optical scan angle was used to achieve a 3.23 mm linear scan field. The polygon scanner we used is capable of rotation speed of 7,000 – 30,000 revolutions per minute (RPM), i.e., 1.4 kHz – 6 kHz line rate. Polygon scanner with even higher rotation speed, e.g., 55,000 RPM, is possible from different manufacturers, potentially further increasing the scan speed to 11 kHz line rate.

For hippocampus activity imaging (Fig. 3d), a 5 mm-aperture non-conjugated galvo-galvo scanner (Saturn 9B, ScannerMax) was used since the FOV was small. This configuration shared the same lenses and effective excitation NA (Supplementary Fig. 2) as the polygon-galvo configuration. The galvo-galvo scanner could achieve ~ 1 kHz line rate at ~ 40-degree peak-to-peak optical scan angle.

A fast remote focusing module (Fig. 1) enabled tuning of the 2P focal plane away from the 3P focal plane. In the 2P beam path, an HWP (WPH05M-915, Thorlabs) and PBS (PBS255, Thorlabs) directed the beam onto a quarter wave plate (QWP) and the remote focusing objective (ROBJ) (LMH-50X-850, Thorlabs). The QWP and ROBJ were double passed after reflection from a small mirror (PF03-03-P01) and a custom-made adapter (~ 20 g total weight), which were mounted on a voice coil (LFA 2010; Equipment Solutions). The back aperture of the ROBJ was conjugated to the back aperture of the imaging objective. The axial resolution at different focal plane positions during remote focusing is shown in Supplementary Fig. 13.

For signal collection, the fluorescence and third harmonic generation (THG) signal were epi-collected through the imaging objective lens and immediately reflected by a 77 mm × 108 mm dichroic beam splitter (FF705-Di01, Semrock) to a detection system (Special Optics, Navitar) that was custom-designed to achieve a high collection efficiency. Another 77 mm × 108 mm dichroic mirror (FF470-Di01, Semrock) split the signal into two channels: one for the fluorescence signal emitted from GCaMP6s and the other for the THG signal. One-inch optical filters 520/70 (FF01-520/70, Semrock) and 435/40 (FF02-435/40, Semrock) were used for the fluorescence and THG channels, respectively. The signals were detected with two 14 × 14 mm^2 effective sensor area GaAsP photomultiplier tube (H15460-40) that was customized for low dark-count and with the built-in preamplification unit removed. The detection efficiency of the system was estimated to be ~ 3.5% for fluorescence imaging across the 3.5 mm FOV at an imaging depth of 900 μm. The detection efficiency was calculated using an established empirical model [41] for the fluorescence profile on the brain surface and the measurement result in Supplementary Fig. 12.

The PMT current was converted to voltage by a transimpedance amplifier (HCA-200 M-20 K-C, Femto). Analog-to-digital conversion was done by a data acquisition card at a sampling clock of 123 MHz (vDAQ, Vidrio). Light shielding was carefully done to achieve a dark count of ~ 1000 photons per second under the usual imaging environment. The acquisition system achieved shot-noise-limited performance. 3P signals for the two beamlets were acquired with two acquisition gates for time demultiplexing. A customized ScanImage 2021 (Vidrio) running on Matlab (MathWorks) was used to place the 3P signals from each beamlet into two virtual channels. These channels were interleaved with a custom Matlab script after image acquisition. 2P signal was placed into a separate virtual channel. A translation stage was used to move the sample (M-285, Shutter Instrument). For depth measurement, the slightly larger index of refraction in brain tissue relative to water resulted in a slight underestimate (5–10%) of the actual imaging depth within the tissue, because the imaging depths reported here are the raw axial movement of the sample [39].

Two-photon and three-photon temporal multiplexing. Simultaneous 2P and 3P excitation were achieved by temporal multiplexing of the 920 nm Ti:Sapphire laser and the 1320 nm Spirit-NOPA. The setup is similar to the one described in a previous study [15]. Briefly, the two excitation beams were combined with a 980 nm long pass dichroic mirror (DMLP1000R, Thorlabs) and passed through the same scanners. They were spatially separated into different focal planes by using the remote focusing module. The 920 nm laser was intensity modulated with an EOM, which was controlled by a transistor-transistor logic (TTL) gate signal. The TTL signal was generated from a signal generator (SDG2042X, Siglent) that was triggered by the Spirit-NOPA laser. The EOM had high transmission for 360 ns between two adjacent Spirit-NOPA laser pulses (or pulse pairs for the two beamlets) that were ~ 500 ns apart.

Adaptive excitation. A structural image was first obtained from conventional raster scanning. Then Gaussian filters and median filters were used to remove sharp features in the image. The regions for imaging were selected by using the top 80% of pixel intensity in the structural image, which effectively excludes regions of the blood vessel shadows. The positions of the areas for imaging were then converted into a digital time sequence for each scan line and sent to an arbitrary waveform generator (AWG). The AWG, triggered by the line trigger from ScanImage, controlled a Pockels cell to transmit laser power only to the selected areas within the FOV. Adaptive excitation for 3PE was achieved with one AWG (PXI-5412, National Instrument). Adaptive excitation for 2P/3P multiplexing was achieved with two AWGs (PXI-5421 and PXI-5412, National Instrument) to accommodate different selected areas at different imaging depths. The AWGs were configured to have a sampling rate of 5 MHz. For 3PM, the time sequence from the AWG was directly sent to the Pockels cell driver (302A, Conoptics). For 2PM, the time sequence from the AWG was combined with the TTL gate signal (see the section on *Two-photon and three-photon temporal multiplexing*) with an AND gate (TI SN74HC08N, Texas Instruments) before sending it to the Pockels cell driver (25D, Conoptics) (Supplementary Fig. 14).

Sampling Scheme: The sampling scheme of the microscope is synchronized with the Spirit-NOPA system. The laser system triggers the acquisition card at 1.96 MHz, with a 63 × electronic multiplier added, resulting in a sampling rate of 123.48 MHz. The frame rate is primarily determined by the pixel binning factor and the number of pixels per frame. During polygon scanning, a line clock is generated using an 852-nm laser illumination (LP852-SF30, Thorlabs) directed at the polygon and detected by a photodiode (DET10A2, Thorlabs), operating independently from the acquisition card. (Supplementary Fig. 15).

Image acquisition parameters. All acquisition parameters for structural and functional imaging are summarized in Supplementary Table 2. The comparison with other multiphoton microscopes that are capable of simultaneous 2P and 3P imaging is in Supplementary Table 3.

4.2 Image processing for structural recording

In Supplementary Video 1, Video 2, Video 5 and Video 6, structural images were normalized by linear transform of pixel intensities to saturate the brightest 0.1–0.5% pixels in each frame. Three-dimensional reconstruction of the stacks was rendered in Imaris (Oxford Instruments).

4.3 Image processing and data analysis for activity recording

Motion corrections were performed using Suite2p [42]. Neuron segmentation was done using Suite2p or manually with ImageJ. Extractions of fluorescence time traces (F) were done with Suite2p or a custom Matlab script. Traces (F) were filtered with a moving average of window size of 2 s. Baselines of the traces (F_0) were determined by excluding the spikes and their rising and falling edges. Traces (F) were normalized according to the formula $(F\text{-}F_0)/F_0$.

For the visual representation of calcium activities in Supplementary Video 3, the raw image sequence was processed by Kalman filter with a gain of 0.7. For Supplementary Video 4, the raw image sequence was processed by moving average of 4 frames and Kalman filter with a gain of 0.8 (left) and by DeepCAD [43] (right).

4.4 Excitation efficiency optimization using discriminability index (d')

The d' for calcium transient detection using the beamlet scanning schemes (Supplementary Fig. 3) was calculated according to equations for three-photon excited fluorescence in a Gaussian focus [22, 44]. All calculations were performed assuming a spherical region of interest (ROI) with a radius of 5 μm. Excitation inside the ROI yields a fluorescence signal while excitation outside the ROI yields background. To maximize power efficiency, we assumed 100% labeling density to penalize excitation outside the ROI and to reduce neuropil contamination. The refractive index of the medium was 1.33. The center wavelength was 1320 nm and the laser pulse width was 60 fs (FWHM). Three-photon cross-section of GCaMP6s (3×10^{-82} cm^6s^2) was used. The fluences calculated assuming diffraction-limited focus and Gaussian beam focus are indicated in Supplementary Fig. 3.

4.5 Animal surgery and in vivo calcium imaging of awake mice

All animal experiments and housing procedures were conducted in accordance with Cornell University Institutional Animal Care and Use Committee guidance. Chronic craniotomy was performed on mice according to the procedures described in the previous work [15]. Briefly, a window of 5-mm diameter was created, centering at ~ 2.5 mm lateral and ~ 2 mm caudal from the bregma point over the somatosensory cortex. Calcium imaging was performed on transgenic animals with GCaMP6s-expressing neurons (male and female, 15–18 weeks, *CamKII-tTA/tetO-GCaMP6s*). Imaging of spontaneous calcium activity was performed on awake animals 2–8 weeks post-cranial window implantation on a treadmill (Mouse Treadmill with Encoder, LABmaker). Deuterium oxide (D_2O) was used as the immersion liquid under the objective lens to maximize power transmission.

4.6 Vasculature imaging for resolution measurement

The mice were anesthetized with isoflurane (1–1.5% in oxygen, with breathing frequency maintained at 1 Hz) and placed on a heat blanket to maintain body temperature at 37.5 °C. Eye ointment was applied. The vasculature of the transgenic mouse (*TIT2L-GC6s-ICL-tTA2*, female, 25-week-old) was labeled via retro-orbital injection of fluorescein (25 mg of dextran conjugate dissolved in 200 mL of sterile saline, 70-kDa molecular weight; D1823, Invitrogen). Distilled water was used as the immersion liquid under the objective.

4.7 Animal surgery and in-vivo calcium imaging of zebrafish

Adult zebrafish (*Danio rerio*) (*Tg(elavl3::H2B-GCaMP6s)*), male, 9 months postfertilization [45] were used for whole-brain imaging. Small to medium-sized fish were chosen, and the standard length (tip of the head to the base of tail) is approximately 15.4 mm. Zebrafish were anesthetized with 0.2 mg mL^{-1} tricaine solution (pH 7.2). Then 2 mL pancuronium bromide (0.4 mg mL^{-1} in Hanks) was retro-orbitally injected to paralyze the fish. The fish was then transferred to a petri dish with a 'V'-shaped mounting putty (Loctite) to support the fish with the dorsal side up. A drop of the anesthetic bupivacaine was placed on the head. A small strip of putty was gently placed over the back of the fish to secure it. Fish were perfused through the mouth with an ESI MP2 Peristaltic Pump (Elemental Scientific) at a rate of 2 mL min^{-1} with oxygenated fish system water during the experiment. The oxygenated fish system water also acts as the immersion liquid under the objective.

Abbreviations

2PM	Two-photon microscopy
3PM	Three-photon microscopy
AWG	Arbitrary waveform generator
CA1	Cornu Ammonis 1 (a region in the hippocampus)
DEEPscope	Dual Excitation with adaptive Excitation Polygon-scanning multiphoton microscope
DM	Dichronic mirror
EC	External capsule
EOM	Electro-optical modulators
FOV	Field of view

FWHM	Full-width half maximum
L	Lens
L6	Layer 6
LFOV	Large field of view
M	Mirror
Mux	Multiplexing
NA	Numerical aperture
NOPA	Noncollinear optical parametric amplifier
OBJ	Objective
PBS	Polarizing beam splitter cube
PSF	Point spread function
QWP	Quarter wave plate
ROBJ	Remote focusing objective
RPM	Revolutions per minute
SL	Scan lens
SP	Stratum pyramidale
t_{delay}	Time delay between the pulses of the two beamlets
THG	Third harmonic generation
TL	Tube lens
VC	Voice coil

Supplementary Information

The online version contains supplementary material available at https://doi.org/10.1186/s43593-024-00076-4.

Supplementary material 1

Acknowledgements
We thank members of the Xu research group, especially Bo Li, Xusan Yang, and Kibaek Choe for their help and valuable discussions. We thank Spencer Smith and Che-Hang Yu for the discussion of optics design. We thank Katherine Strednak, Emily Silvela, and Faith Burgus from Cornell Center for Animal Resources and Education for their animal care service. We thank Karl Termini from the Cornell glass shop for his help in glass grinding. We thank Robert Page, Stanley McFall, Chris Cowulich, and Jeffrey Koski from the Cornell machine shop for their help in machining. We thank the Cornell Institute of Biotechnology for providing a workstation for 3D rendering. We thank Vidrio, Special Optics, Nidec Copal Electronics, Hamamatsu Photonics, ScannerMax, and AVR optics for customized parts.

Author contributions
Conceptualization: AM, TW, CX. Methodology: AM, TW, SZ, DGO, CS, CW, CX. Investigation: AM, KEK, JF, DW, CX. Visualization: AM. Supervision: CX. Writing—original draft: AM. Writing—review & editing: AM, TW, CX.

Funding
National Science Foundation NeuroNex (Grant No. DBI-1707312 to C.X.). NIH/NINDS (Grant No. U01NS103516 to C.X.). Cornell Neurotech Mong Fellowship to A.M.

Availability of data and materials
The datasets used and/or analyzed during the current study are available from the corresponding author on reasonable request.

Declarations

Ethics approval and consent to participate
Not applicable.

Competing interests
C.X., A.M., T.W., are listed as inventors on a US provisional patent application (serial no. 63/464,489) on Optical Pulse Generator and Method. The other authors declare no competing interests.

Received: 23 June 2024 Revised: 28 August 2024 Accepted: 20 September 2024
Published online: 01 November 2024

References

1. N.J. Sofroniew, D. Flickinger, J. King, K. Svoboda, A large field of view two-photon mesoscope with subcellular resolution for in vivo imaging. Elife **5**, e14472 (2016)
2. C.H. Yu, Y. Yu, L.M. Adsit, J.T. Chang, J. Barchini, A.H. Moberly, H. Benisty, J. Kim, B.K. Young, K. Heng, D.M. Farinella, A. Leikvoll, R. Pavan, R. Vistein, B.R. Nanfito, D.G.C. Hildebrand, S. Otero-Coronel, A. Vaziri, J.L. Goldberg, A.J. Ricci, D. Fitzpatrick, J.A. Cardin, M.J. Higley, G.B. Smith, P. Kara, K.J. Nielsen, I.T. Smith, S.L.V. Smith, The Cousa objective: a long-working distance air objective for multiphoton imaging in vivo. Nat. Methods **21**, 132–141 (2024)
3. S. Weisenburger, F. Tejera, J. Demas, B. Chen, J. Manley, F.T. Sparks, F. Martínez Traub, T. Daigle, H. Zeng, A. Losonczy, A. Vaziri, Volumetric Ca2+ imaging in the mouse brain using hybrid multiplexed sculpted light microscopy. Cell **177**, 1–17 (2019)
4. J. Demas, J. Manley, F. Tejera, K. Barber, H. Kim, F.M. Traub, B. Chen, A. Vaziri, High-speed, cortex-wide volumetric recording of neuroactivity at cellular resolution using light beads microscopy. Nat. Methods **18**, 1103–1111 (2021)
5. C.H. Yu, J.N. Stirman, Y. Yu, R. Hira, S.L. Smith, Diesel2p mesoscope with dual independent scan engines for flexible capture of dynamics in distributed neural circuitry. Nat. Commun. **12**, 1–13 (2021)
6. K. Ota, Y. Oisi, T. Suzuki, M. Ikeda, Y. Ito, T. Ito, H. Uwamori, K. Kobayashi, M. Kobayashi, M. Odagawa, C. Matsubara, Y. Kuroiwa, M. Horikoshi, J. Matsushita, H. Hioki, M. Ohkura, J. Nakai, M. Oizumi, A. Miyawaki, T. Aonishi, T. Ode, M. Murayama, Fast, cell-resolution, contiguous-wide two-photon imaging to reveal functional network architectures across multi-modal cortical areas. Neuron **109**, 1–15 (2021)
7. O.I. Rumyantsev, J.A. Lecoq, O. Hernandez, Y. Zhang, J. Savall, R. Chrapkiewicz, J. Li, H. Zeng, S. Ganguli, M.J. Schnitzer, Fundamental bounds on the fidelity of sensory cortical coding. Nature **580**, 100–105 (2020)
8. R. Lu, Y. Liang, G. Meng, P. Zhou, K. Svoboda, L. Paninski, N. Ji, Rapid mesoscale volumetric imaging of neural activity with synaptic resolution. Nat. Methods **17**, 291–294 (2020)
9. J.N. Stirman, I.T. Smith, M.W. Kudenov, S.L. Smith, Wide field-of-view, multi-region, two-photon imaging of neuronal activity in the mammalian brain. Nat. Biotechnol. **34**, 857–862 (2016)
10. M. Clough, I.A. Chen, S.-W. Park, A.M. Ahrens, J.N. Stirman, S.L. Smith, J.L. Chen, Flexible simultaneous mesoscale two-photon imaging of neural activity at high speeds. Nat. Commun. **12**, 1–7 (2021)
11. P.S. Tsai, C. Mateo, J.J. Field, C.B. Schaffer, M.E. Anderson, D. Kleinfeld, Ultra-large field-of-view two-photon microscopy. Opt. Express **23**, 13833–13847 (2015)
12. F.K. Janiak, P. Bartel, M.R. Bale, T. Yoshimatsu, E. Komulainen, M. Zhou, K. Staras, L.L. Prieto-Godino, T. Euler, M. Maravall, T. Baden, Non-telecentric two-photon microscopy for 3D random access mesoscale imaging. Nat. Commun. **13**, 544 (2022)
13. K. Takasaki, R. Abbasi-asl, J. Waters, Superficial bound of the depth limit of two- photon imaging in mouse brain. eNeuro **7**, 1–10 (2020)
14. M. Yildirim, H. Sugihara, P.T.C. So, M. Sur, Functional imaging of visual cortical layers and subplate in awake mice with optimized three-photon microscopy. Nat. Commun. **10**, 177 (2019)
15. D.G. Ouzounov, T. Wang, M. Wang, D.D. Feng, N.G. Horton, J.C. Cruz-Hernández, Y.-T. Cheng, J. Reimer, A.S. Tolias, N. Nishimura, C. Xu, In vivo three-photon imaging of activity of GCaMP6-labeled neurons deep in intact mouse brain. Nat. Methods **14**, 388–390 (2017)
16. M.A. Thornton, G.L. Futia, M.E. Stockton, S.A. Budoff, A.N. Ramirez, B. Ozbay, O. Tzang, K. Kilborn, A. Poleg-Polsky, D. Restrepo, E.A. Gibson, E.G. Hughes, Long-term in vivo three-photon imaging reveals region-specific differences in healthy and regenerative oligodendrogenesis. Nat. Neurosci. **27**, 846–861 (2024)
17. T. Wang, C. Xu, Three-photon neuronal imaging in deep mouse brain. Optica **7**, 947–960 (2020)

18. Y. Hontani, F. Xia, C. Xu, Multicolor three-photon fluorescence imaging with single-wavelength excitation deep in mouse brain. Sci. Adv. **7**, 3531–3548 (2021)
19. C. Zhao, S. Chen, L. Zhang, D. Zhang, R. Wu, Y. Hu, F. Zeng, Y. Li, D. Wu, F. Yu, Y. Zhang, J. Zhang, L. Chen, A. Wang, H. Cheng, Miniature three-photon microscopy maximized for scattered fluorescence collection. Nat. Methods **20**, 617–622 (2023)
20. A. Klioutchnikov, D.J. Wallace, J. Sawinski, K.M. Voit, Y. Groemping, J.N.D. Kerr, A three-photon head-mounted microscope for imaging all layers of visual cortex in freely moving mice. Nat. Methods **20**, 610–616 (2023)
21. A. Klioutchnikov, D.J. Wallace, M.H. Frosz, R. Zeltner, J. Sawinski, V. Pawlak, K.M. Voit, P.S.J. Russell, J.N.D. Kerr, Three-photon head-mounted microscope for imaging deep cortical layers in freely moving rats. Nat. Methods **17**, 509–513 (2020)
22. C. Xu, W.W. Webb, Multiphoton excitation of molecular fluorophores and nonlinear laser microscopy, in *Topics in fluorescence spectroscopy*. ed. by J.R. Lakowicz (Springer, 2002), pp.471–540
23. Y. Li, S.J. Montague, A. Brüstle, X. He, C. Gillespie, K. Gaus, E.E. Gardiner, W.M. Lee, High contrast imaging and flexible photomanipulation for quantitative in vivo multiphoton imaging with polygon scanning microscope. J. Biophotonics **11**, 1–12 (2018)
24. Y.X. Li, V. Gautam, A. Brüstle, I.A. Cockburn, V.R. Daria, C. Gillespie, K. Gaus, C. Alt, W.M. Lee, Flexible polygon-mirror based laser scanning microscope platform for multiphoton in-vivo imaging. J. Biophotonics **10**, 1526–1537 (2017)
25. B. Li, C. Wu, M. Wang, K. Charan, C. Xu, An adaptive excitation source for high-speed multiphoton microscopy. Nat. Methods **17**, 163–166 (2020)
26. B.A. Wilt, J.E. Fitzgerald, M.J. Schnitzer, Photon shot noise limits on optical detection of neuronal spikes and estimation of spike timing. Biophys. J. **104**, 51–62 (2013)
27. D.M. Chow, D. Sinefeld, K.E. Kolkman, D.G. Ouzounov, N. Akbari, R. Tatarsky, A. Bass, C. Xu, J.R. Fetcho, Deep three-photon imaging of the brain in intact adult zebrafish. Nat. Methods **17**, 605–608 (2020)
28. N. Akbari, R.L. Tatarsky, K.E. Kolkman, J.R. Fetcho, A.H. Bass, C. Xu, Whole-brain optical access in a small adult vertebrate with two- and three-photon microscopy. iScience **25**, 105191 (2022)
29. K. Choe, Y. Hontani, T. Wang, E. Hebert, D.G. Ouzounov, K. Lai, A. Singh, W. Béguelin, A.M. Melnick, C. Xu, Intravital three-photon microscopy allows visualization over the entire depth of mouse lymph nodes. Nat. Immunol. **23**, 330–340 (2022)
30. G.J. Bakker, S. Weischer, J.F. Ortas, J. Heidelin, V. Andresen, M. Beutler, E. Beaurepaire, P. Friedl, Intravital deep-tumor single-beam 3-photon, 4-photon, and harmonic microscopy. Elife **11**, 1–23 (2022)
31. H.A. Bounds, M. Sadahiro, W.D. Hendricks, M. Gajowa, K. Gopakumar, D. Quintana, B. Tasic, T.L. Daigle, H. Zeng, I.A. Oldenburg, H. Adesnik, Ultra-precise all-optical manipulation of neural circuits with multifunctional Cre-dependent transgenic mice. bioRxiv (2022). https://doi.org/10.1101/2021.10.05.463223
32. H. Dana, Y. Sun, B. Mohar, B.K. Hulse, A.M. Kerlin, J.P. Hasseman, G. Tsegaye, A. Tsang, A. Wong, R. Patel, J.J. Macklin, Y. Chen, A. Konnerth, V. Jayaraman, L.L. Looger, E.R. Schreiter, K. Svoboda, D.S. Kim, High-performance calcium sensors for imaging activity in neuronal populations and microcompartments. Nat. Methods **16**, 649–657 (2019)
33. Y. Zhang, M. Rózsa, Y. Liang, D. Bushey, Z. Wei, J. Zheng, D. Reep, G.J. Broussard, A. Tsang, G. Tsegaye, S. Narayan, C.J. Obara, J.-X. Lim, R. Patel, R. Zhang, M.B. Ahrens, G.C. Turner, S.S.-H. Wang, W.L. Korff, E.R. Schreiter, K. Svoboda, J.P. Hasseman, I. Kolb, L.L. Looger, Fast and sensitive GCaMP calcium indicators for imaging neural populations. bioRxiv (2021). https://doi.org/10.1101/2021.11.08.467793
34. D. Li, Z. Hu, H. Zhang, Q. Yang, L. Zhu, Y. Liu, T. Yu, J. Zhu, J. Wu, J. He, P. Fei, W. Xi, J. Qian, D. Zhu, A Through-Intact-Skull (TIS) chronic window technique for cortical structure and function observation in mice. eLight **2**, 15 (2022). https://doi.org/10.1186/s43593-022-00022-2
35. Y.J. Zhao, T.T. Yu, C. Zhang, Z. Li, Q.M. Luo, T.H. Xu, D. Zhu, Skull optical clearing window for in vivo imaging of the mouse cortex at synaptic resolution. Light Sci. Appl. **7**, 17153 (2018)
36. C. Zhang, W. Feng, Y. Zhao, T. Yu, P. Li, T. Xu, Q. Luo, D. Zhu, A large, switchable optical clearing skull window for cerebrovascular imaging. Theranostics **8**, 2696–2708 (2018)
37. G. Silasi, D. Xiao, M.P. Vanni, A.C.N. Chen, T.H. Murphy, Intact skull chronic windows for mesoscopic wide-field imaging in awake mice. J. Neurosci. Methods **267**, 141–149 (2016)
38. A. Steinzeig, D. Molotkov, E. Castrén, Chronic imaging through "transparent skull" in mice. PLoS ONE **12**, e0181788 (2017)
39. T. Wang, D.G. Ouzounov, C. Wu, N.G. Horton, B. Zhang, C.H. Wu, Y. Zhang, M.J. Schnitzer, C. Xu, Three-photon imaging of mouse brain structure and function through the intact skull. Nat. Methods **15**, 789–792 (2018)
40. Z. Qin, Z. She, C. Chen, W. Wu, J.K.Y. Lau, N.Y. Ip, J.Y. Qu, Deep tissue multiphoton imaging using adaptive optics with direct focus sensing and shaping. Nat. Biotechnol. **40**, 1663–1671 (2022)
41. E. Beaurepaire, J. Mertz, Epifluorescence collection in two-photon microscopy. Appl. Opt. **41**, 5376–5382 (2002)
42. M. Pachitariu, C. Stringer, M. Dipoppa, S. Schröder, L.F. Rossi, H. Dalgleish, M. Carandini, K.D. Harris, Suite2p: beyond 10,000 neurons with standard two-photon microscopy. bioRxiv (2017). https://doi.org/10.1101/061507
43. X. Li, G. Zhang, J. Wu, Y. Zhang, Z. Zhao, X. Lin, H. Qiao, H. Xie, H. Wang, L. Fang, Q. Dai, Reinforcing neuron extraction and spike inference in calcium imaging using deep self-supervised denoising. Nat. Methods **18**, 1395–1400 (2021)
44. T. Wang, C. Wu, D.G. Ouzounov, W. Gu, F. Xia, M. Kim, X. Yang, M.R. Warden, C. Xu, Quantitative analysis of 1300-nm three-photon calcium imaging in the mouse brain. Elife **9**, e53205 (2020)
45. N. Vladimirov, Y. Mu, T. Kawashima, D.V. Bennett, C.T. Yang, L.L. Looger, P.J. Keller, J. Freeman, M.B. Ahrens, Light-sheet functional imaging in fictively behaving zebrafish. Nat. Methods **11**, 883–884 (2014)